Multiscale analysis of multilayer printed circuit board using Mechanics of Structure Genome

Fei Tao[a], Xiuqi Lyu[b], Xin Liu[a], Wenbin Yu[a]

[a]*School of Aeronautics and Astronautics, Purdue University, West Lafayette, IN 47907-2045, USA*
[b]*Department of Systems Innovation, School of Engineering, The University of Tokyo, Tokyo, 113-8654 Japan*

Abstract

The structure of Printed Circuit board (PCB) is very complicated because it consists of woven composites and custom defined conducting layers. To improve the reliability of PCB, it is critical to predict the constitutive relations accurately. This study by implementing Mechanics of Structure Genome (MSG), homogenizes a multilayer PCB to determine the effective mechanical properties and coefficient of thermal expansions (CTEs). The homogenization is divided into two steps. The first step is to obtain the yarn material properties. The second is to write python script in TexGen4SC to generate the woven model and combine it with conducting layers in ABAQUS to obtain the PCB effective material properties. A new tool, which is freely accessible at cdmHUB, was developed to integrate the two steps woven homogenization. The homogenized material properties were validated with representative volume element (RVE) analysis. A good agreement was observed between MSG and RVE analysis. Finally, both structural analysis and dehomogenization were done to predict a PCB plate global responses and local stress fields. MSG-based plate structural analysis and dehomogenization matched the direct numerical simulation (DNS) very well. However, MSG is significantly faster than DNS.

Keywords: Multilayer PCB, Woven Composites, Mechanics of Structure Genome, Homogenization, Constitutive modeling

Email address: `wenbinyu@purdue.edu` (Wenbin Yu)

1. Introduction

The printed circuit board (PCB), a multilayer structure, has been used in almost all electronic devices. The principal uses of PCB are to act as the primary structure to support all components in a circuit and to include the copper wiring to connect the electronics components. During the service life, PCB endures a wide range of loads, such as thermal load, vibration, and fatigue. Nevertheless, the requirements of PCB are to have a more complex circuit, thinner thickness and higher performance over the same or smaller size [1]. These requirements pose challenges to the reliability of PCB. Currently, the design of PCB relies on board level tests [2], such as three-point bending test [3], which are expensive and time-consuming. Besides, the board tests can only present the global response, with the local behaviors, such as local failure initiation and stresses distribution, remaining unknown [4]. However, simulations are able to predict both global and local response effectively, it is necessary to run simulations to determine the most reliable design in order to evaluate different design scenarios effectively and avoid the defective prototypes at the early stage.

A microstructure of a PCB is shown in Figure 1. As it shows, the PCB is the combination of copper wiring and woven composites consisting of matrix and glass fiber [5]. The majority of work regards the PCB as a simplified single layer board with isotropic material properties [6, 7] which did not consider the complex microstructure of woven composites and conducting layer. This simplification is not accurate enough for further analysis, i.e. reliability analysis. Hence, in order to evaluate different design scenarios effectively and avoid the defective prototypes at the early stage, it is necessary to predict the PCB constitutive relations and local stresses accurately.

A great number of analytical models have been proposed to study the woven composites. Ishikawa and Chou [8, 9] proposed models which are based on the Classical Lamination Theory (CLT) and the assumptions of iso-strain or iso-stress condition. Among these models, the Mosaic model provides the upper and lower bounds of the in-plane material properties. Naik [10] proposed models that are based on the mixed iso-strain or iso-stress conditions. The in-plane material properties of these models were validated with experimental results. Gommers [11] applied the Mori-Tanaka inclusion method to different types of textile composites, which yields better results than the classical iso-strain model. Although they can provide a good estimation of the in-plane material properties, analytical models are not able
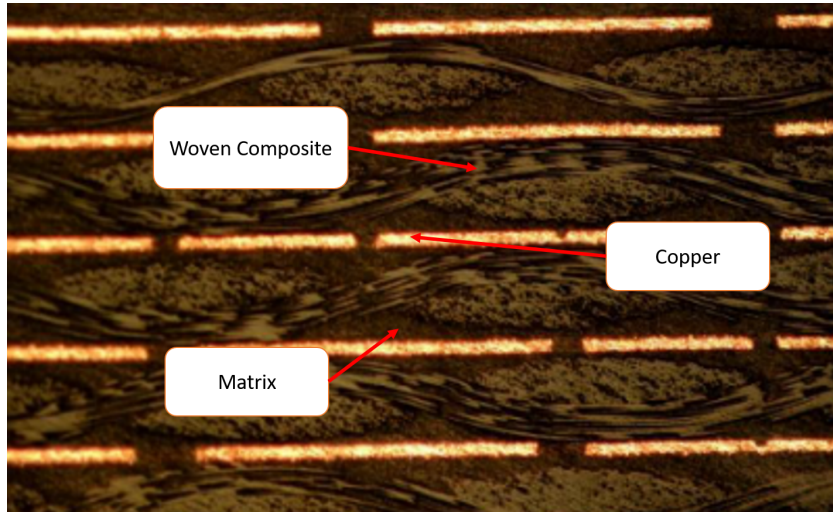
Figure 1: The microstructure of PCB

to accurately predict the transverse material properties of woven composites. Besides, analytical models have their own limitation. It is difficult to find a unified model that can deal with all the scenarios of the woven composites.

Computational models are another kind of strategy to analyze the effective properties of woven composites. Usually, the microstructure of the woven composites will be discretized using finite elements. Then, the numerical methods will be applied to compute the effective properties [12]. In general, computational models produce better results in comparison with analytical models. In addition, computational models are also able to predict the local stress and strain fields through dehomogenization which can be applied in the failure analysis [13]. The representative volume element (RVE) analysis, which uses the Finite Element Analysis (FEA), is a very popular method in the woven composites analysis. For example, some researchers used RVE analysis to study the non-metallic woven composites thermo-mechanical response [14], determined the composite beam flexural properties [15], examined the effective properties of multilayer composites containing both metallic and woven composite plies [16]. Girard applied RVE to a 3D woven composites used in PCB for high-frequency application [17]. Chen determined the material properties of multilayer PCB with woven composites [18]. However, the RVE analysis is computationally expensive when the microstructure of the woven composites is complex. Additionally,

3

it is not straightforward to apply periodic boundary conditions (PBCs) for an RVE. Mechanics of structure genome (MSG), a semi-analytical method, that significantly reduces the computational costs and keeps the accuracy as FEA [19]. This approach is based on the principle of minimum information loss (PMIL), which introduces no ad hoc assumptions and guarantees the accuracy of the results [20]. MSG has been demonstrated to be an effective tool for the linear and nonlinear analysis of various 2D and 3D woven composites [21, 20]. MSG has been coded into a general-purpose constitutive modeling software SwiftComp, which is able to perform homogenization and dehomogenization of different engineering structures with complex geometry made of anisotropic materials [22].

This paper aims at using MSG to develop a two steps multi-scale approach to homogenize the multilayer PCB to determine the effective mechanical properties and CTEs. The MSG-based structural analysis and dehomogenization were then carried out to predict the global responses and local stresses. For the homogenization, firstly, the yarn material properties were obtained by a squared-packed model with MSG. Then, use TexGen4SC, which integrated TexGen [23] and SwiftComp, to generate a woven model and combine it with the copper layer. Finally, determine the multilayer PCB material properties with MSG. The results from MSG were validated with the RVE analysis. The MSG-based structural analysis and dehomogenization results were compared with DNS.

2. Materials of PCB

The conducting layers of PCB usually have a very complex and aperiodic structure, since different customers have different requirements and needs. Some researchers ignored this layer or regarded the conducting layer as pure copper. However, in view of significant difference of Youngs modulus and CTEs between copper and matrix, the thermal effect is critical in the analysis of PCB. Regarding the fact that the conducting layer is not pure copper, in this paper, a regular copper design is adopted to simplify the analysis. The design of the conducting layer is shown in Figure 2. In this figure, the bright color represents the copper, the dark color the matrix .

The PCB insulating materials consist of matrix and reinforced woven composites. The matrix, typically epoxy resin, is the dominant material that affects the CTEs. The material properties of woven composites are influenced not only by the fiber and matrix properties but also by the fabric counts and
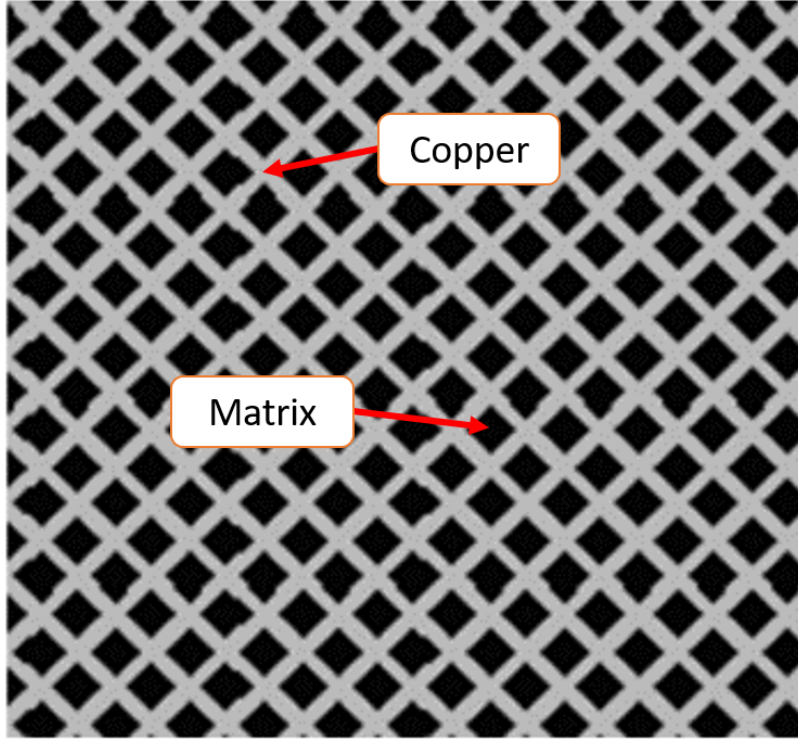
Figure 2: The conducting layer of a PCB [1]

the yarn geometry. The fabric types of the PCB are classified by the IPC (the Association Connecting Electronics Industries) standard [24]. In this study, we chose the 1080 fabric type, which is a 2D plain-weaved woven composite commonly used in PCB, for the purposes of demonstration. The warp and weft counts of the fabric are 23.6×18.5 per centimeter respectively. The fiber counts are 200 per yarn. The fiber is 0.005 mm in diameter. The width and thickness of the warp are 0.208 mm and 0.04 mm, while the width and thickness of the weft are 0.315 mm and 0.028 mm. The size of the unit cell for the conducting layer was chosen as 0.84 mm $\times$ 1.08 mm $\times$ 0.01 mm, which has the same length and width as that of woven unit cell. The copper volume fraction was chosen as 0.54. The yarn fiber volume fraction (V_f) were calculated by using fiber area divided yarn area. The material properties of the fiber, matrix, and copper are summarized in Table 1.

Table 1: PCB constituent material properties

	E (GPa)	ν	CTEs ($\mu/°$C)
Fiber	73.00	0.21	16.23
Resin	6.00	0.33	40.11
Copper	121.00	0.34	16.00

3. MSG-based multi-scale modeling approach to PCB

3.1. MSG theory for homogenization

The analysis domain of MSG is structure genome (SG), which is the smallest mathematical material block of a structure. SG can be chosen as 1D, 2D or 3D domain depending on the heterogeneity of a structure. SG works similar to RVE concept in micromechanics for 3D models. However, there are significant differences between SG and RVE. For example, the analysis over the 1D or 2D SG can predict the complete set of solid properties and local fields. However, this cannot be achieved by either 1D and 2D RVE using the finite element analysis.

The MSG can be formulated by minimizing the information loss between the original heterogeneous body and imaginary homogenized body. For a linear elastic material, the information can be strain energy density. Defining the macro coordinate as x_i and the micro coordinate as y_i, these two coordinates are related by using the equation $y_i = x_i/\delta$, where δ is a small parameter that describes SG. Hence with MSG, we can express the kinematics of the original heterogeneous body in terms of the imaginary homogeneous body as

$$u_i(x, y) = \bar{u}_i(x) + \delta\chi_i(x, y) \tag{1}$$

where u_i is the displacement of the original heterogeneous body; $\bar{u}_i$ is the displacement of the homogenized body; χ_i represents the fluctuating function which refers to the difference between the two fields.

Therefore the strain fields of the heterogeneous body can be written as

$$\varepsilon_{ij}(x, y) = \bar{\varepsilon}_{ij}(x) + \chi_{(i,j)} \tag{2}$$

where $\bar{\varepsilon}_{ij}(x) = \frac{1}{2}\left(\frac{\partial \bar{u}_i}{\partial x_j} + \frac{\partial \bar{u}_j}{\partial x_i}\right)$ is the strain field of the homogenized body. The subscript represents the operation as $A_{(i,j)} = \frac{1}{2}\left(\frac{\partial A_i}{\partial y_j} + \frac{\partial A_j}{\partial y_i}\right)$. The kinematic

6

variables of the homogenized body in terms of the original model can be defined as

$$\bar{u}_i = \langle u_i \rangle \quad \bar{\varepsilon}_{ij} = \langle \varepsilon_{ij} \rangle \tag{3}$$

where $\langle \cdot \rangle$ represents the volume average over the domain. The equations above imply the following constraints on the fluctuating functions

$$\langle \chi_i \rangle = 0 \quad \langle \chi_{(i,j)} \rangle = 0 \tag{4}$$

The strain energy difference between the original model and the homogenized model is

$$\Pi = \left\langle \frac{1}{2} C_{ijkl} \varepsilon_{ij} \varepsilon_{kl} + \beta_{ij} \varepsilon_{ij} \theta + \frac{1}{2} c_v \frac{\theta^2}{T_0} \right\rangle - \left\langle \frac{1}{2} C^*_{ijkl} \bar{\varepsilon}_{ij} \bar{\varepsilon}_{kl} + \bar{\beta}_{ij} \bar{\varepsilon}_{ij} \theta + \frac{1}{2} \bar{c}_v \frac{\theta^2}{T_0} \right\rangle = 0 \tag{5}$$

where C_{ijkl} represents the components of the fourth-order elasticity tensor, β_{ij} are components of the second-order tensor of thermal stress coefficients, c_v is the specific heat per unit volume at constant volume, T_0 is the reference temperature at which the constituent material is stress free, θ denotes the difference between the actual temperature and the reference temperature. We assume that θ is constant with respect to time and space coordinates, which is a common practice in the literature.

Regarding the homogenized model as given (i.e. C^*_{ijkl} and $\bar{\varepsilon}_{ij}$ cannot be varied), the minimization of Π yields the following variation statement

$$\min_{\chi_i \in \text{Eq.(4)}} \left\langle \frac{1}{2} C_{ijkl} \varepsilon_{ij} \varepsilon_{kl} + \beta_{ij} \varepsilon_{ij} \theta + \frac{1}{2} c_v \frac{\theta^2}{T_0} \right\rangle =$$
$$\min_{\chi_i \in \text{Eq.(4)}} \left\{ \left\langle \frac{1}{2} C_{ijkl} \left(\bar{\varepsilon}_{ij} + \chi_{(i,j)} \right) \left(\bar{\varepsilon}_{kl} + \chi_{(k,l)} \right) \right\rangle + \left\langle \beta_{ij} \left(\bar{\varepsilon}_{ij} + \chi_{(i,j)} \right) \right\rangle + \left\langle \frac{1}{2} c_v \frac{\theta^2}{T_0} \right\rangle \right\} \tag{6}$$

Denoting $\bar{\varepsilon} = \begin{bmatrix} \bar{\varepsilon}_{11} & \bar{\varepsilon}_{22} & \bar{\varepsilon}_{33} & 2\bar{\varepsilon}_{23} & 2\bar{\varepsilon}_{13} & 2\bar{\varepsilon}_{12} \end{bmatrix}$ and $w = \begin{bmatrix} \chi_1 & \chi_2 & \chi_3 \end{bmatrix}$. Then the function of the variational statement of Eq. (6) can be written in the following form as

$$U = \frac{1}{2} \left\langle (\Gamma_h w + \bar{\varepsilon})^T C (\Gamma_h w + \bar{\varepsilon}) \right\rangle + \left\langle \beta (\Gamma_h w + \bar{\varepsilon}) \theta \right\rangle + \frac{1}{2} \left\langle c_v \frac{\theta^2}{T_0} \right\rangle \tag{7}$$

with

$$\Gamma_h = \begin{bmatrix} \frac{\partial}{\partial y_1} & 0 & 0 \\ 0 & \frac{\partial}{\partial y_2} & 0 \\ 0 & 0 & \frac{\partial}{\partial y_3} \\ 0 & \frac{\partial}{\partial y_3} & \frac{\partial}{\partial y_2} \\ \frac{\partial}{\partial y_3} & 0 & \frac{\partial}{\partial y_1} \\ \frac{\partial}{\partial y_2} & \frac{\partial}{\partial y_1} & 0 \end{bmatrix} \tag{8}$$

For a 3D SG, with the finite element method, we can express w using shape functions defined over SG as

$$w(x_k, y_j) = S(y_j)V(x_k) \tag{9}$$

where S is the standard shape function which depends on the type of elements one uses; V is the nodal value which needs to be solved for fluctuating functions.

Substituting Eq. (9) into Eq. (7), we can obtain the discretized version of the strain energy function

$$U = \frac{1}{2}(V^T E V + 2V^T D_{h\varepsilon}\bar{\varepsilon} + \bar{\varepsilon}^T D_{\varepsilon\varepsilon}\bar{\varepsilon} + 2V^T D_{h\theta}\theta + 2\bar{\varepsilon}^T D_{\varepsilon\theta}\theta + D_{\theta\theta}\frac{\theta^2}{T_0}) \tag{10}$$

where

$$\begin{aligned} E = \left\langle (\Gamma_h S)^T C (\Gamma_h S) \right\rangle \quad D_{h\varepsilon} = \left\langle (\Gamma_h S)^T C \right\rangle \quad D_{\varepsilon\varepsilon} = \langle C \rangle \\ D_{h\theta} = \left\langle (\Gamma_h S)^T \beta \right\rangle \quad D_{\varepsilon\theta} = \langle \beta \rangle \quad D_{\theta\theta} = \langle c_v \rangle \end{aligned} \tag{11}$$

Minimizing U in Eq. (10) subject to constraints gives the following linear system

$$EV = -D_{h\varepsilon}\bar{\varepsilon} - D_{h\theta}\bar{\theta} \tag{12}$$

The above equation shows that V linearly depends on $\bar{\varepsilon}$ and θ. Therefore, the solution to V can be symbolically written as

$$V = V_0\bar{\varepsilon} + V_\theta\theta \tag{13}$$

With Eq. (13) being substituted into Eq. (10), the strain energy stored in the SG is shown as

$$\begin{aligned} U = \frac{1}{2}\bar{\varepsilon}^T(V_0^T D_{h\varepsilon} + D_{\varepsilon\varepsilon})\bar{\varepsilon} + \bar{\varepsilon}^T \left[\frac{1}{2}(D_{h\varepsilon}^T V_\theta + V_0^T D_{h\theta}) + D_{\varepsilon\theta}\right]\theta \\ + \frac{1}{2}(V_\theta^T D_{h\theta}T_0 + D_{\theta\theta})\frac{\theta^2}{T_0} \equiv \frac{1}{2}\bar{\varepsilon}^T C^* \bar{\varepsilon} + \bar{\varepsilon}^T \beta^* \theta + \frac{1}{2}c_v^*\frac{\theta^2}{T_0} \end{aligned} \tag{14}$$

8

where C^* represent the effective stiffness matrix, β^* is the effective thermal stress coefficient, c_v^* is the effective specific heat.

The effective coefficient of thermal expansion is

$$\alpha^* = -(C^*)^{-1}\beta^* \tag{15}$$

The fluctuating function can be obtained as

$$w = S(V_0\bar{\varepsilon} + V_\theta\theta) \tag{16}$$

The local displacement can be obtained as

$$u_i = \bar{u}_i + x_\alpha(C_{\alpha i} - \delta_{\alpha i}) + \varepsilon w_j C_{ji} \tag{17}$$

where u_i is the local displacement, $\bar{u}_i$ the macroscopic displacement. Since SG has coordinates y_k with corresponding x_k in the macroscopic structural model , $\bar{u}_i$ should be expressed as

$$\bar{u}_i = \bar{u}_i(x_{k_0}) + x_k\bar{u}_{i,k} \tag{18}$$

where x_{k_0} is the center of the SG and $\bar{u}_{i,k}$ is the gradient along x_k evaluated correspond to x_{k_0}.

The local strain can be obtained as

$$\varepsilon = \Gamma_h S(V_0\bar{\varepsilon} + V_\theta\theta) + \bar{\varepsilon} \tag{19}$$

The local stresses can be obtained in accordance with Hook's law as

$$\sigma = C\varepsilon + \beta\theta \tag{20}$$

This paper also used MSG-based Kirchhoff-Love plate model analysis. The formulation for the plate model is shown in Appendix A.

3.2. Modeling framework of PCB

The MSG modeling of PCB can be divided into three steps: homogenization (micro-scale and macro-scale), structural analysis and dehomogenization as shown in Figure 3.
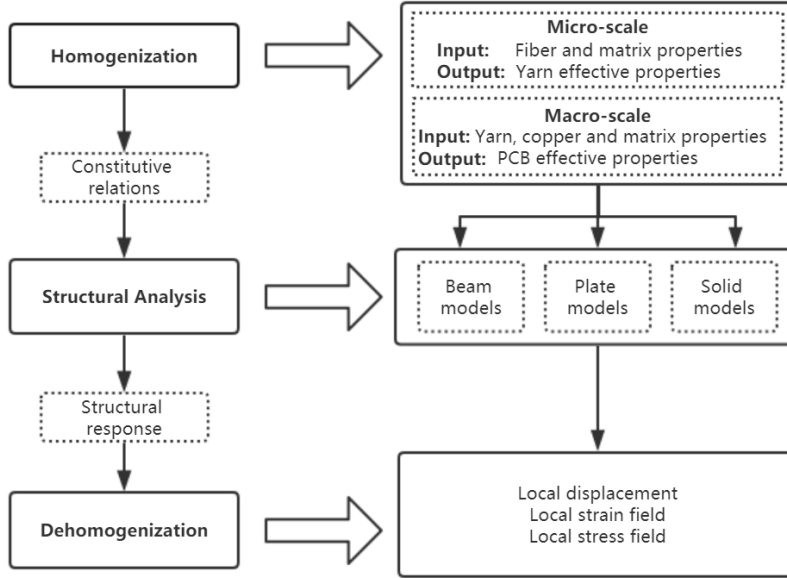
Figure 3: MSG analysis flow chart

3.2.1. PCB homogenization

The first step of the MSG homogenization of woven composites reinforced PCB is to identify the SG of yarn. As the yarn is heterogeneous over the cross section and uniform along the yarn path, a 2D square-packed SG has been identified for the yarn homogenization. The 2D SG is shown in Figure 4. Although the domain of the SG is 2D, the strain energy is expressed in 3D field. Thus, MSG can provide the complete set of the solid effective material properties. The result from MSG will be compared with a 3D RVE model.

The next step is to do the macro homogenization to obtain the constitutive relations of PCB. TexGen4SC was used to generate the woven model. Currently, TexGen4SC graphic user interface (GUI) cannot create the woven composite with different warp and weft cross section. A python script has been written to create the woven model with different cross section between warp and weft. The script is accessible at cdmHUB [25]. The voxel mesh was used in TexGen4SC to avoid distorted elements. However, voxel mesh requires a large number of elements to obtain accurate representation of the woven composite geometry. Therefore, a convergence study was carried out to determine the mesh size of the woven model. A new tool was developed to integrate the two steps homogenization, which significantly improved the
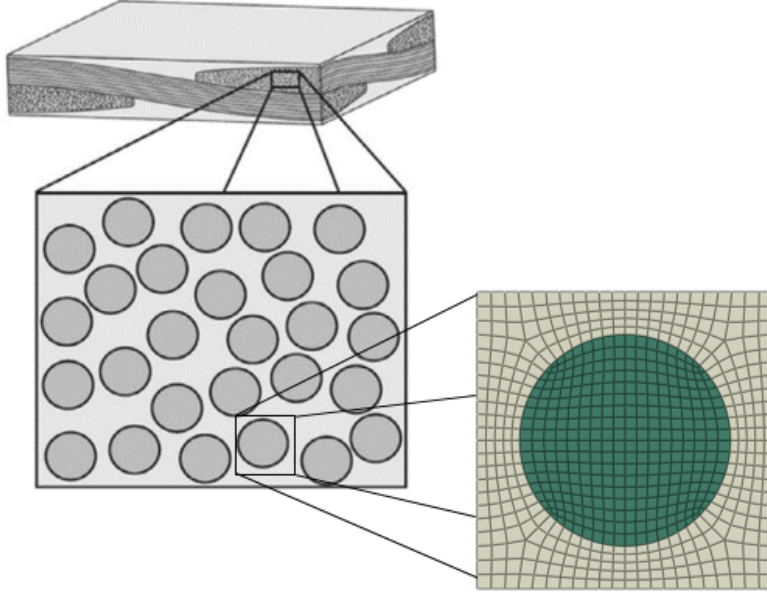
Figure 4: Square packed SG of the yarn [14]

efficiency of determining the PCB fabric type at the design stage. The new tool is freely accessible at cdmHUB [25]. The woven model was then exported to Abaqus and merged with the conducting layers at both the top and the bottom. Thus, a double-sided PCB model had been created. The length and width of the PCB are the same as those of woven SG, which are 1.08 mm and 0.84 mm, respectively. The thickness is 0.1 mm. The building process is summarized in Figure 5. MSG can also predict the constitutive relations in the form of beam stiffness matrix or plate stiffness matrix. The predicted beam stiffness matrix or the plate stiffness matrix can be directly used for the 1D beam or 2D plate analysis. This paper used 3D solid model and 2D plate model to capture the constitutive relations of the PCB. Note for a double-sided PCB, the periodicity does not exist in the y_3 direction. Applying periodic boundary conditions to all the directions will make the material stiffer, resulting in larger Young's modulus. Partial aperiodic boundary conditions (y_3 direction) should be chosen for a more accurate prediction for effective material properties. It can easily be done with MSG. In this paper, both the periodic and partially aperiodic scenarios are investigated.
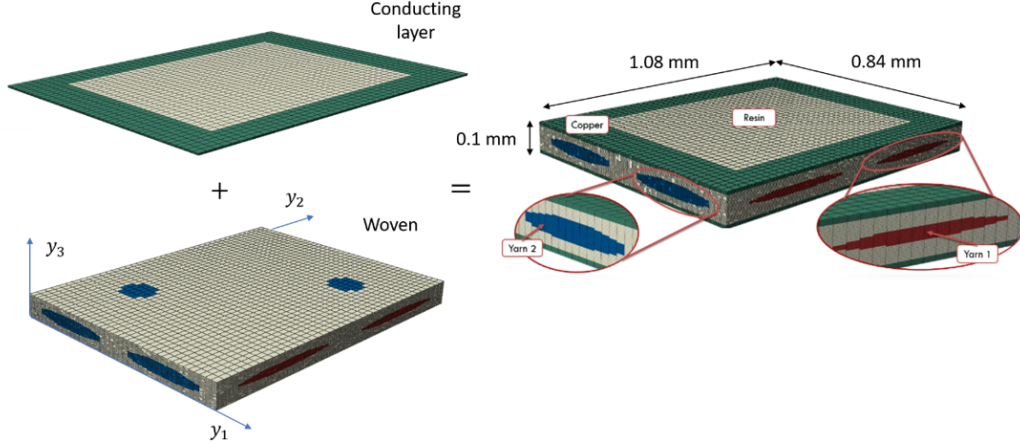
11

Figure 5: The SG of PCB

3.2.2. PCB structural analysis and dehomogenization

After the homogenized constitutive relations are obtained, we need to evaluate whether the homogenized properties are satisfactory or not. One can compare the structural responses of the model using homogenized properties and the original material properties to evaluate the homogenized properties. For the purpose of demonstration, this paper examined the stress and displacement fields in a double-sided PCB plate which is shown in Figure 6. This plate was built by duplicating the PCB SG 10 times along the length and width direction. Therefore, the length, width and hight of the plate is 10.8 mm × 8.4 mm × 0.1 mm. The plate is fixed at one end and subject to 100 KPa pressure on the top surface. The model was discretized into about 6 million C3D8 elements. The DNS was done to be the reference case. The analysis was also done for the model which had the same dimension as the DNS but with homogenized constitutive relations.

The MSG-based dehomogenization can provide the local stresses and strains, which can be used for further analysis, like that of fatigue. The input to perform dehomogenization is the average global displacements and global strains. The average strain can be computed from the structural analysis. The local strains and stresses are obtained from Eqs. (19) and (20), respectively. The local stresses were compared with the DNS for validation.
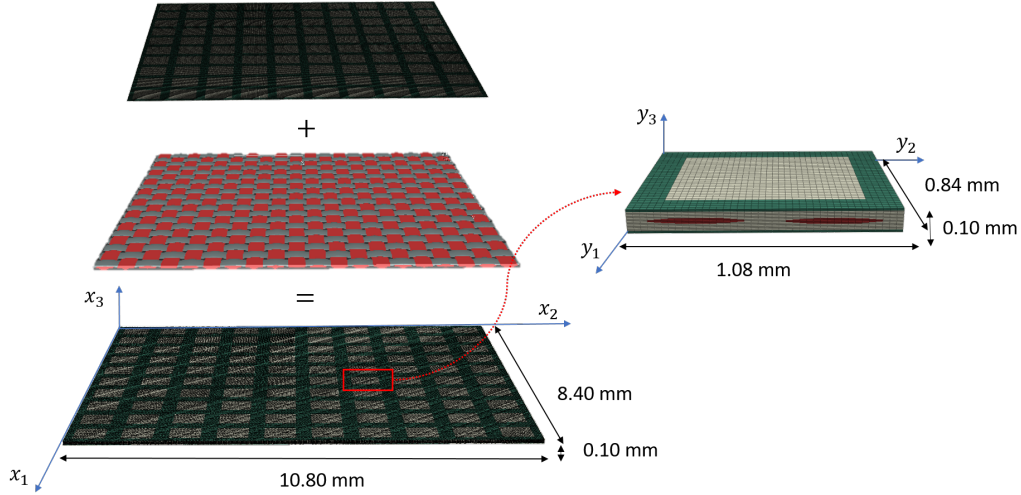
12

Figure 6: DNS model of PCB

4. Results and discussion

Based on the yarn information provided in section 2. The warp and weft V_f were calculated as 0.54 and 0.41 respectively. The effective properties of the yarn were computed based on the 2D squared packed SG as shown in Figure 4. Table 2 presents the warp and weft effective properties from MSG and RVE with PBCs applied to all the three directions. Diff 1 and Diff 2 represent the difference between MSG and RVE analysis of warp and weft respectively. As one can observe from the table, the nine engineering constants and CTEs computed using MSG matches very well with 3D RVE results, the differences within 1 %. However, MSG is about 8 times faster than 3D FEA. Besides, this table also presents that the Young's modulus and shear modulus of warp are larger than those of the weft. But CTEs of warp are smaller than that of weft. This difference is caused by the different fiber volume fraction V_f between warp and weft, because fiber has larger Young's modulus and smaller coefficient of thermal expansion in terms of matrix. The larger V_f of the warp results in larger Young's modulus and shear modulus compare with weft.

Before the homogenization of PCB was carried out, a convergence study was done to determine the mesh size of the woven SG. E_2 was chosen as the parameter to determine whether the result converges or not. Figure 7 presents the convergence study result. It shows that the model converges

13

Table 2: Effective properties of Yarn

Effective Properties	MSG Warp	RVE Warp	MSG Weft	RVE Weft	Diff 1	Diff 2
E_1(GPa)	42.21	42.32	33.13	33.12	-0.26%	-0.03%
E_2(GPa)	18.40	18.38	13.30	13.34	0.11%	0.30%
E_3(GPa)	18.40	18.38	13.30	13.34	0.11%	0.30%
G_{23}(GPa)	4.88	4.85	3.86	3.87	0.61%	0.26%
G_{13}(GPa)	6.35	6.38	4.72	4.70	-0.47%	-0.42%
G_{12}(GPa)	6.35	6.38	4.72	4.70	-0.47%	-0.42%
ν_{23}	0.27	0.27	0.32	0.32	0.00%	0.94%
ν_{13}	0.26	0.26	0.27	0.27	-0.77%	0.74%
ν_{12}	0.26	0.26	0.27	0.27	-0.77%	0.74%
$\alpha_{11}(\mu/^\circ\text{C})$	17.94	17.83	18.94	18.87	0.61%	0.39%
$\alpha_{22}(\mu/^\circ\text{C})$	28.23	28.10	32.20	32.24	0.46%	-0.12%
$\alpha_{33}(\mu/^\circ\text{C})$	28.23	28.10	32.20	32.24	0.46%	-0.12%

when the number of nodes reaches 52,111. The homogenized material properties of the woven are presented in Table 3. Diff 1 is the difference between MSG aperiodic and RVE. Diff 2 represents the difference between MSG and RVE. The result shows that all the engineering constants and CTEs from MSG (periodic) agree well with RVE analysis. Besides, one can also observe that the Young's modulus of MSG Aperiodic is smaller than that of MSG and RVE. This is expected, as the periodic conditions in the y_3 makes the material stiffer.

Table 4 presents the solid effective properties of the PCB computed from MSG and RVE analysis. Again, Diff 1 is the difference between MSG aperiodic and RVE. Diff 2 represents the difference between MSG and RVE. Similarly, one can observe that all the engineering constants and CTEs from MSG agree well with RVE analysis, and MSG Aperiodic Young's modulus is smaller than RVE. However, MSG is approximately 10 times faster than RVE analysis. Besides, when comparing PCB with woven composites, one can observe that the Young's modulus and shear modulus are significantly larger than the woven composites. In view of the fact that the conducting layer is just 0.01 mm in thickness, it indicates that the conducting layer can significantly influence the PCB behavior.

The none-zero components of the plate stiffness matrix are $A_{11} = 2.02 \times 10^3$ N/mm, $A_{22} = 2.22 \times 10^3$ N/mm, $A_{12} = A_{21} = 4.52 \times 10^2$ N/mm, $A_{66} =$

Table 3: Effective properties of woven

Effective Properties	MSG Aperiodic	MSG	RVE	Diff 1	Diff 2
E_1(GPa)	13.44	13.91	13.99	-3.93%	-0.57%
E_2(GPa)	15.22	15.6	15.74	-3.30%	-0.89%
E_3(GPa)	9.37	9.47	9.55	-1.88%	-0.84%
G_{23}(GPa)	3.09	3.10	3.12	-0.96%	-0.64%
G_{13}(GPa)	3.04	3.04	3.06	-0.65%	-0.65%
G_{12}(GPa)	3.48	3.49	3.51	-0.85%	-0.57%
ν_{23}	0.32	0.32	0.32	0.00%	0.00%
ν_{13}	0.34	0.34	0.34	0.00%	0.00%
ν_{12}	0.20	0.19	0.19	5.26%	0.00%
$\alpha_{11}(\mu/^{\circ}\text{C})$	23.83	23.81	23.53	1.27%	1.19%
$\alpha_{22}(\mu/^{\circ}\text{C})$	20.52	20.73	20.54	-0.10%	0.93%
$\alpha_{33}(\mu/^{\circ}\text{C})$	41.38	41.32	40.96	1.03%	0.88%

Table 4: Effective properties of PCB

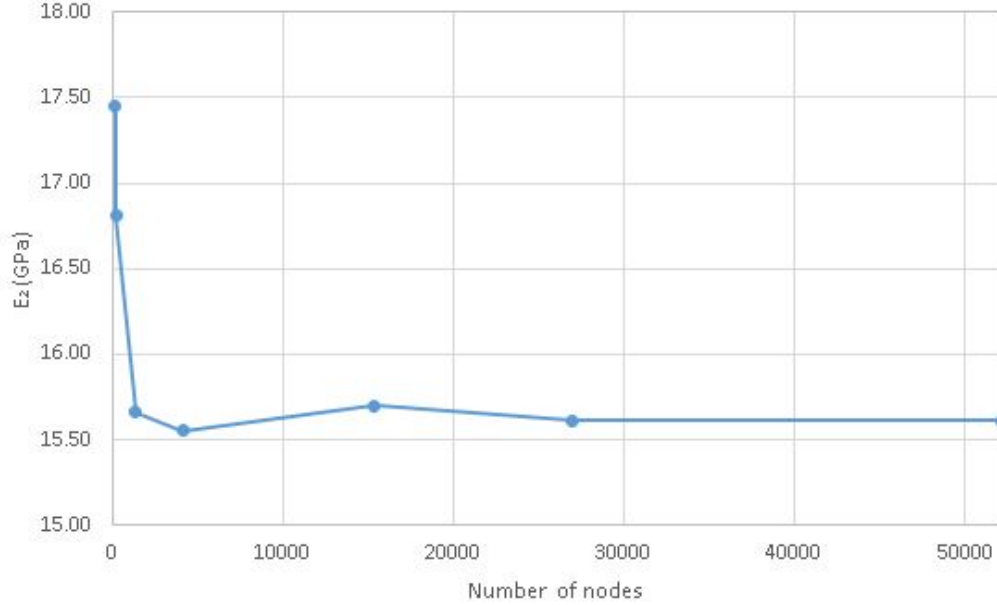| Effective Properties	MSG Aperiodic	MSG	RVE	Diff 1	Diff 2
E_1(GPa)	19.56	19.75	19.77	-1.06%	-0.10%
E_2(GPa)	21.21	21.38	21.37	-0.75%	0.05%
E_3(GPa)	10.07	10.30	10.27	-1.95%	0.29%
G_{23}(GPa)	3.20	3.24	3.23	-0.93%	0.31%
G_{13}(GPa)	3.15	3.19	3.18	-0.94%	0.31%
G_{12}(GPa)	4.97	4.97	4.97	0.00%	0.00%
ν_{23}	0.33	0.33	0.33	0.00%	0.00%
ν_{13}	0.34	0.34	0.34	0.00%	0.00%
ν_{12}	0.20	0.20	0.20	0.00%	0.00%
$\alpha_{11}(\mu/^{\circ}\text{C})$	21.43	21.52	21.50	-0.33%	0.09%
$\alpha_{22}(\mu/^{\circ}\text{C})$	19.71	19.84	19.87	-0.81%	-0.15%
$\alpha_{33}(\mu/^{\circ}\text{C})$	42.78	42.06	42.19	1.40%	-0.31%

Figure 7: Convergence study of woven SG

4.97×10^1 N/mm, $D_{22} = 2.21$ N·mm, $D_{12} = D_{21} = 4.01 \times 10^{-1}$ N·mm, $D_{66} = 7.23 \times 10^{-1}$ N·mm, which were used in the 2D macroscopic plate analysis. The outputs, global displacement and curvatures, were used in the MSG-based dehomogenization to get local stress and strain fields.

Figure 8 presents the global displacement $\bar{u}_3$ along x_2 axis. The result shows an excellent match between DNS and MSG-based plate model. The difference of displacement at the tip of plate between these two approaches is 0.52 %. In addition, there is little difference between MSG-based solid model with periodic and aperiodic conditions. However, one can observe a significant difference between DNS and MSG-based solid model at the tip. The difference reaches 28.46 %. This indicates MSG-based plate model predicts more accurate result than solid model for this bending problem of PCB.
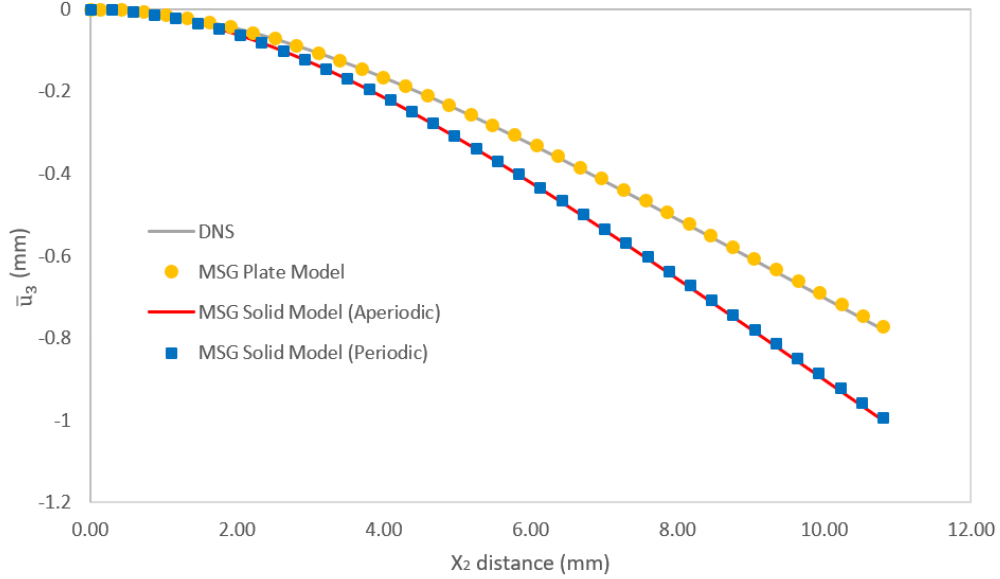
16

Figure 8: The comparison of $\bar{u}_3$ of four different models

Figure 9 shows the stress fields of σ_{11}, σ_{22} and σ_{12} through the thickness of the PCB plate. The stress fields were plotted at $x_1 = 4.4$ mm, $x_2 = 5.64$ mm, $x_3 = 0 - 0.10$ mm. The result indicates that the differences of DNS and MSG dehomogenization are acceptable. Note that the accuracy can be improved by converting the linear element into quadratic element, like the C3D20 brick element. However, the computation cost of the DNS can be extremely expensive. The author's computation resources is not adequate for DNS using quadratic elements. Hence, in this study, only the examined SG used quadratic elements. Overall, MSG has captured all the trends and discontinuities of the stresses distribution. However, MSG is much more efficient than DNS, as the dehomogenization took only 5 mins with 1 CPU, while DNS took 36 hours with 100 CPUs.

17

(a) σ_{11}

(b) σ_{22}
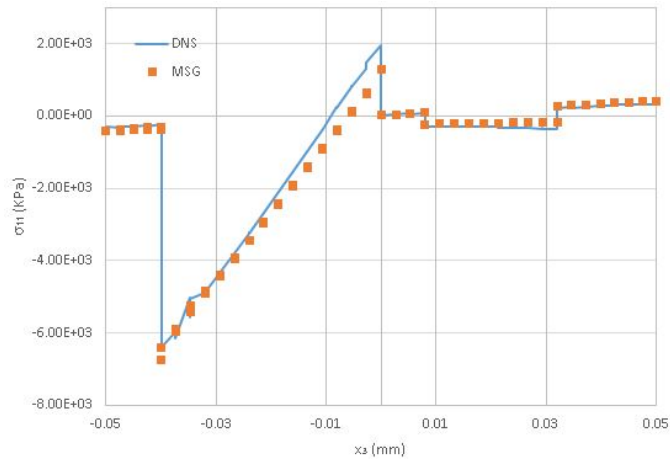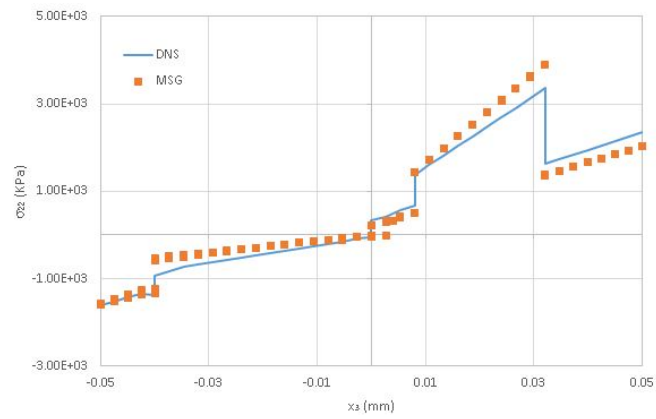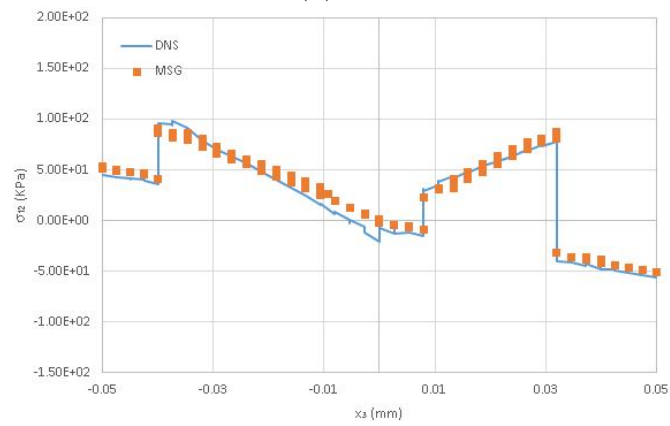
(c) σ_{12}

Figure 9: Stress fields in PCB through thickness

5. Conclusion

In this paper, the MSG was employed to do the homogenization, structural analysis, and dehomogenization of a multilayer woven composites reinforced PCB. This approach simplified the original complicated structural analysis into constitutive modeling and macroscopic structural analysis, keeping the accuracy of the analysis and improving the efficiency significantly. As for the homogenization of PCB with MSG, it has been divided into two steps. The first step is to homogenize the yarn based on the fabric information of the yarn and fiber and matrix properties. The second step is to compute the PCB constitutive relations with the homogenized yarn, matrix, and copper. A tool was developed to integrate the two steps homogenization. The homogenized solid properties from MSG show good agreements with RVE analysis. However, the Young's modulus is larger as the periodic conditions in the y_3 direction makes the material stiffer. With regard to the structural analysis, it shows the MSG-based plate analysis predicted global response better than the analysis using solid homogenized properties. Thus, it is better to use the plate constitutive relations to conduct PCB structural analysis instead of using homogenized solid properties. Finally, MSG dehomogenization predicted the local stress fields fairly well in comparison with DNS. However, MSG dehomogenizaiton approach is much more efficient than DNS. Overall, this research work has shown the capability of MSG to predict the multilayer PCB constitutive relations and structural responses. This novel approach can be an effective tool in the design and analysis of PCB.

Appendix A. MSG-based Kirchhoff-Love plate model

To derive the Kirchhoff-Love plate model using MSG, the 3D displacement field can be expressed in terms of the 2D displacement variables admit-

ted by the Kirchhoff-Love plate model as:

$$u_1(x_1, x_2, y_1, y_2, y_3) = \bar{u}_1(x_1, x_2) - \delta y_3 \bar{u}_{3,1}(x_1, x_2) + \delta w_1(x_1, x_2, y_1, y_2, y_3)$$
$$u_2(x_1, x_2, y_1, y_2, y_3) = \bar{u}_2(x_1, x_2) - \delta y_3 \bar{u}_{3,2}(x_1, x_2) + \delta w_2(x_1, x_2, y_1, y_2, y_3)$$
$$u_3(x_1, x_2, y_1, y_2, y_3) = \bar{u}_3(x_1, x_2) + \delta w_3(x_1, x_2, y_1, y_2, y_3)$$

$$(A.1)$$

Where u_i and $\bar{u}_i$ denote the displacements of the original 3D heterogeneous structure and the 2D plate model respectively. Plate displacements are functions of x_1 and x_2. w_1, w_2, and w_3 are unknown fluctuating functions which need to be solved. In this formulation, there are no apriori assumptions about the kinematics such as the commonly invoked Kirchhoff-Love assumptions. The introduction of the fluctuating functions enables to describe all the possible displacements for every material point of a plate-like structure made of textile composites, which cannot be adequately expressed by the simple kinematics of the Kirchhoff-Love model.

By dropping the small terms based on variation asymptotically method (VAM), the 3D strain filed can be expressed as

$$
\begin{aligned}
\varepsilon_{11} &= \epsilon_{11} + \delta y_3 \kappa_{11} + w_{1|1} \\
\varepsilon_{22} &= \epsilon_{22} + \delta y_3 \kappa_{22} + w_{2|2} \\
\varepsilon_{33} &= w_{3|3} \\
2\varepsilon_{12} &= 2\epsilon_{12} + 2\delta y_3 \kappa_{12} + w_{1|2} + w_{2|1} \\
2\varepsilon_{13} &= w_{1|3} + w_{3|1} \\
2\varepsilon_{23} &= w_{2|3} + w_{3|2}
\end{aligned}
\qquad (A.2)
$$

Where the plate strains and curvatures can be defined as

$$\epsilon_{\alpha\beta}(x_1, x_2) = \frac{1}{2}(\bar{u}_{\alpha,\beta} + \bar{u}_{\beta,\alpha}) \quad \kappa_{\alpha\beta}(x_1, x_2) = -\bar{u}_{\alpha\beta} \qquad (A.3)$$

The total potential energy of the 3D structure can be defined as

$$\Pi = \frac{1}{2}\int_s U_{2D} ds - W \qquad (A.4)$$

Where U_{2D} is the 2D strain energy density defind as

$$U_{2D} = \frac{1}{2}\langle \sigma_{ij}\varepsilon_{ij} \rangle = \frac{1}{2}\langle C_{ijkl}\varepsilon_{ij}\varepsilon_{kl} \rangle \qquad (A.5)$$

Following the same procedure as for MSG solid model with the fluctuating functions constraints give

$$\langle w_i \rangle = 0 \tag{A.6}$$

Drop small terms according to VAM and minimize the potential energy. Imposing the constraints for fluctuating functions to solve w_i. The 3D strain filed can be expressed in terms of 2D plate strain and curvatures.

The 2D kinetic variables called plate stress resultants are defined as

$$\frac{\partial U_{2D}}{\partial \epsilon_{11}} = N_{11} \quad \frac{\partial U_{2D}}{\partial \epsilon_{22}} = N_{22} \quad \frac{\partial U_{2D}}{\partial 2\epsilon_{12}} = N_{12}$$
$$\frac{\partial U_{2D}}{\partial \kappa_{11}} = M_{11} \quad \frac{\partial U_{2D}}{\partial \kappa_{22}} = M_{22} \quad \frac{\partial U_{2D}}{\partial 2\kappa_{12}} = M_{12} \tag{A.7}$$

We can get the plate constitutive relation to relate the plate stress resultants and strains and curvatures as

$$
\begin{Bmatrix} N_{11} \\ N_{22} \\ N_{12} \\ M_{11} \\ M_{22} \\ M_{12} \end{Bmatrix} =
\begin{bmatrix}
A_{11} & A_{12} & A_{16} & B_{11} & B_{12} & B_{16} \\
A_{12} & A_{22} & A_{26} & B_{12} & B_{22} & B_{26} \\
A_{16} & A_{26} & A_{66} & B_{16} & B_{26} & B_{66} \\
B_{11} & B_{12} & B_{16} & D_{11} & D_{12} & D_{16} \\
B_{12} & B_{22} & B_{26} & D_{12} & D_{22} & D_{26} \\
B_{16} & B_{26} & B_{66} & D_{16} & D_{26} & D_{66}
\end{bmatrix}
\begin{Bmatrix} \epsilon_{11} \\ \epsilon_{22} \\ 2\epsilon_{12} \\ \kappa_{11} \\ \kappa_{22} \\ 2\kappa_{12} \end{Bmatrix} \tag{A.8}
$$

In Eq. (A.8), the 6×6 plate stiffness matrix is composed of the A, B, and D matrices. Although we used the same notation of A, B, and D from CLPT, the way to obtain it has no relations to that has been used to derive CLPT [19, 26]. The plate stiffness matrix can be directly used in Abaqus or ANSYS to conduct the macroscopic analysis. The formulation of obtaining the plate stiffness matrix and dehomogenization can be found in Yu's paper [26].

References

[1] P. Fuchs, G. Pinter, M. Tonjec, Determination of the orthotropic material properties of individual layers of printed circuit boards, Microelectronics Reliability 52 (2012) 2723–2730.

[2] JESD22-B111A, Board level drop test method of components for handheld electronic products, JEDEC Standard (2016).

[3] ASTM-D790, Standard test methods for flexural properties of unreinforced and reinforced plastics and electrical insulating materials, ASTM International (2017).

[4] C. Le Coq, A. Tougui, M.-P. Stempin, L. Barreau, Optimization for simulation of wl-csp subjected to drop-test with plasticity behavior, Microelectronics Reliability 51 (2011) 1060–1068.

[5] Q. Zhu, P. Shrotriya, N. R. Sottos, P. H. Geubelle, Three-dimensional viscoelastic simulation of woven composite substrates for multilayer circuit boards, Composites science and technology 63 (2003) 1971–1983.

[6] Y. Wang, K. Low, F. Che, H. Pang, S. Yeo, Modeling and simulation of printed circuit board drop test, in: Electronics Packaging Technology, 2003 5th Conference (EPTC 2003), IEEE, pp. 263–268.

[7] Y. Wang, K. Low, H. Pang, K. H. Hoon, F. Che, Y. Yong, Modeling and simulation for a drop-impact analysis of multi-layered printed circuit boards, Microelectronics Reliability 46 (2006) 558–573.

[8] T. Ishikawa, T.-W. Chou, Elastic behavior of woven hybrid composites, Journal of Composite Materials 16 (1982) 2–19.

[9] T. Ishikawa, T.-W. Chou, In-plane thermal expansion and thermal bending coefficients of fabric composites, Journal of Composite Materials 17 (1983) 92–104.

[10] N. Naik, V. Ganesh, Prediction of on-axes elastic properties of plain weave fabric composites, Composites Science and Technology 45 (1992) 135–152.

[11] B. Gommers, I. Verpoest, P. Van Houtte, The mori-tanaka method applied to textile composite materials, Acta Materialia 46 (1998) 2223–2235.

[12] W. Yu, A unified theory for constitutive modeling of composites, Journal of Mechanics of Materials and Structures 11 (2016) 379–411.

[13] G. Nicoletto, E. Riva, Failure mechanisms in twill-weave laminates: Fem predictions vs. experiments, Composites Part A: applied science and manufacturing 35 (2004) 787–795.

[14] Y. Shindo, S. Ueda, Y. Nishioka, Mechanical behavior of woven composites at low temperatures, Fusion Engineering and Design 20 (1993) 469–474.

[15] B. V. Sankar, R. V. Marrey, A unit-cell model of textile composite beams for predicting stiffness properties, Composites science and technology 49 (1993) 61–69.

[16] K. Low, Y. Wang, Hybrid modeling of woven fibre reinforced metal matrix composite for multilayer circuit boards, Circuit World 34 (2008) 12–20.

[17] G. Girard, M. Jrad, S. Bahi, M. Martiny, S. Mercier, L. Bodin, D. Nevo, S. Dareys, Experimental and numerical characterization of thin woven composites used in printed circuit boards for high frequency applications, Composite Structures 193 (2018) 140–153.

[18] Z. Chen, F. Yang, S. Meguid, Multi-level modeling of woven glass/epoxy composite for multilayer printed circuit board applications, International Journal of Solids and Structures 51 (2014) 3679–3688.

[19] X. Liu, K. Rouf, B. Peng, W. Yu, Two-step homogenization of textile composites using mechanics of structure genome, Composite Structures 171 (2017) 252–262.

[20] X. Liu, T. Tang, W. Yu, R. B. Pipes, Multiscale modeling of viscoelastic behaviors of textile composites, International Journal of Engineering Science 130 (2018) 175–186.

[21] K. Rouf, X. Liu, W. Yu, Multiscale structural analysis of textile composites using mechanics of structure genome, International Journal of Solids and Structures (2017).

[22] W. Yu, SwiftComp User Manual, West Lafayette, IN 47907, URL: https://cdmhub.org/resources/scstandard/supportingdocs, 2015.

[23] M. Sherburn, A. Long, Texgen open source project, URL: http://texgen.sourceforge.net (2010).

[24] IPC4412A, Specification for finished fabric woven from E glass for printed boards, IPC, 2008.

[25] F. Tao, Woven composites homogenization integration, URL: https://cdmhub.org/resources/texgendc/supportingdocs (2019).

[26] W. Yu, A unified theory for constitutive modeling of composites, Journal of Mechanics of Materials and Structures 11 (2016) 379–411.